

# Thermodynamic limits of sperm swimming precision.

C. Maggi,\* F. Saglimbeni, V. Carmona Sosa, and R. Di Leonardo

*NANOTEC-CNR, Institute of Nanotechnology, Soft and Living Matter Laboratory, Roma, Italy and  
Dipartimento di Fisica, Sapienza Università di Roma, Piazzale A. Moro 2, I-00185, Rome, Italy.*

B. Nath

*Dipartimento di Fisica, Sapienza Università di Roma, Piazzale A. Moro 2, I-00185, Rome, Italy  
ISC-CNR, Institute for Complex Systems, Piazzale A. Moro 2, I-00185 Rome, Italy and  
Mechanical Engineering Department, National Institute of Technology Silchar, 788010, Assam, India.*

A. Puglisi

*Dipartimento di Fisica, Sapienza Università di Roma, Piazzale A. Moro 2, I-00185, Rome, Italy and  
ISC-CNR, Institute for Complex Systems, Piazzale A. Moro 2, I-00185 Rome, Italy.*

Sperm swimming is crucial to fertilise the egg, in nature and in assisted reproductive technologies. Modelling the sperm dynamics involves elasticity, hydrodynamics, internal active forces, and out-of-equilibrium noise. Here we give experimental evidence in favour of the relevance of energy dissipation for sperm beating fluctuations. For each motile cell, we reconstruct the time-evolution of the two main tail's spatial modes, which together trace a noisy limit cycle characterised by a maximum level of precision  $p_{max}$ . Our results indicate  $p_{max} \sim 10^2 s^{-1}$ , remarkably close to the estimated precision of a dynein molecular motor actuating the flagellum, which is bounded by its energy dissipation rate according to the Thermodynamic Uncertainty Relation. Further experiments under oxygen deprivation show that  $p_{max}$  decays with energy consumption, as it occurs for a single molecular motor. Both observations are explained by conjecturing a high level of coordination among the conformational changes of dynein motors. This conjecture is supported by a theoretical model for the beating of an ideal flagellum actuated by a collection of motors, including a motor-motor nearest neighbour coupling of strength  $K$ : when  $K$  is small the precision of a large flagellum is much higher than the single motor one. On the contrary, when  $K$  is large the two become comparable. Based upon our strong motor coupling conjecture, old and new data coming from different kinds of flagella can be collapsed together on a simple master curve.

## 1. SWIMMING WITH NOISE

Sperm motility plays a crucial role in sexual reproduction and also serves as a prototype for understanding the physics of microswimmers [1, 2]. Its investigation is fundamental to develop new technologies, for instance to improve fertility diagnostics and assisted reproduction techniques [3]. It can also positively influence the field of artificial microswimmers and of microfluidic devices [4].

A sperm cell is composed by a large head (spatulate-shaped for bull sperms as those considered here) and a thin whip-like tail called flagellum, whose oscillatory movement sustains a travelling wave from head to tail [5]. In the last decades, physics has investigated the sperm swimming problem, how it originates from flagellar beating coupled to the fluid dynamics and to the many possible boundary conditions [6–8]. Different swimming modes have been identified, including planar beating near flat (e.g. air-liquid or liquid-substrate) surfaces, beating with precession when the head is anchored to a point, circular trajectories on a plane, 3d helical in the bulk, etc. [9].

In modelling, minimal ingredients for swimming of

semi-flexible filaments, are an anisotropic Stokes drag and a single travelling wave, e.g. (for small deviations  $y(t, s)$  from the straight rod shape at time  $t$  and arclength  $s \sim x$ )  $y(t, x) = A \cos(kx - \omega t)$  which guarantees irreversibility of the shape cycle i.e.  $y(t, x) \neq y(T - t, x)$  where  $T$  is the cycle period, necessary to swim at low Reynolds numbers [10, 11]. An important element is noise, that is deviations from the *average* flagellum beating dynamics, which has been previously considered in modelling [7, 12–14] and in experiments, with *Chlamydomonas* [15–19] and with sperms [20]. In particular such experimental works have estimated through different methods the quality factor of the phase noise in the beating cycle, a parameter which is strictly connected to the precision studied here, as discussed later. Flagellar fluctuations have been observed to influence self-propulsion [21] and synchronization of adjacent filaments [16, 17, 22].

In the present study we show how energy dissipation, an intrinsic quantity for motors at all scales, affects noise in sperm beating, rationalising the problem under the framework of Thermodynamic Uncertainty Relations (TURs) [23–25] (see Appendix D for a summary of the simplest working principle behind TURs). Remarkably, the connection between power consumption and macroscopic fluctuations leads us to put forward a hypothesis about the collective dynamics of the molecular motors

---

\*claudio.maggi@roma1.infn.it

actuating the flagellum.

The sperm axoneme hosts an array of dynein molecules for a total of  $N \sim 10^5$  motor domains [26–28]. Each motor converts available ATP molecules into power strokes inducing local bending of the axoneme. Deviations from the average biochemical cycle of a molecular motor occur mainly because of fluctuating times of residence in the different chemical states [29]. Less understood is the mechanism of coordination of the  $N$  motors necessary to generate the tail’s travelling wave: a widely accepted fact is the presence of some feedback mechanism inducing activation and de-activation of the motors based upon the local bending state [30]. The hypothesis that a dynein operates independently of its neighbors is questioned by the observation - in micrographs by scanning electron microscopy, etc. - of non-random grouping of dynein states and by the evidence that interactions between adjacent dyneins may be inevitable because of the size of dynein arms [31–33]. Our experimental observations about the high amplitude of the noise affecting flagellum beating (comparable to that of a dynein motor) and about the decay of flagellum precision with energy consumption (similar to what happens for a single motor), contribute together to conjecture a strong coupling between the dynamics of adjacent motors proteins. A stylised model for axonemal oscillations under the effect of noisy motor dynamics corroborates our hypothesis.

## 2. PRECISION OF A BROWNIAN MOTOR

We first discuss how to measure “precision”, an observable which has recently attracted a profound interest in non-equilibrium statistical physics, see Fig. 1. For our purpose it is sufficient to consider a system where an angular observable  $\theta(t)$  represents the system’s configuration (see Fig. 1a and b). We expect  $\theta(t)$  to perform an irreversible stochastic stationary dynamics with average drift  $\langle \theta(t) - \theta(0) \rangle = Jt$  and relative dispersion  $\langle [\theta(t) - \theta(0) - Jt]^2 \rangle \sim 2Dt$  for large  $t$ . We are interested in the precision rate defined as

$$p = \frac{J^2}{D}. \quad (1)$$

The observable  $p$  can be understood as the inverse of the typical time  $t^* = 1/p$  separating the diffusive regime  $t \ll t^*$  ( $Dt \gg (Jt)^2$ ) from the ballistic regime  $t \gg t^*$  (see Fig. 1c and its insets).

The quantity  $p$  has been demonstrated - through the so-called Thermodynamic Uncertainty Relation (TUR) [23–25] to be bounded from above by the entropy production rate, or in practical terms (for the purpose of steady isothermal molecular motors) the motor’s energy consumption rate  $\dot{W}$  in thermal units:

$$p \leq p_{TUR} = \frac{\dot{W}}{k_B T}. \quad (2)$$

The ratio  $\mathcal{Q} = p/p_{TUR} \leq 1$  can be considered as a motor’s figure of merit. Estimates of  $p$  through Markovian models informed by experimental data [34] suggest that several molecular motors work not far from their optimum, or at least close to its order of magnitude ( $\mathcal{Q} \geq 0.1$ ). In the following we present a method to estimate  $p$  and we apply it to experiments with bulls’ sperm cells (see Fig. 1b and d). Notwithstanding its physical relevance, the quantity  $p$  has not been discussed for microswimmers, even if its estimate can be deduced from other variables in previous works. Quantities which are strictly related to  $p$  are the dissipation time [35] and the quality factor  $q = J/(2D) = p/(2J)$ , which has been measured within a similar approach for *Chlamydomonas* flagella in [15–19] and for bull sperms in [20], although never compared to energy dissipation and or discussed within the framework of TURs.

## 3. PRECISION OF SPERM BEATING

We adopt a coarse-graining protocol that reduces the space of possible shapes of the flagellum into two coordinates, the minimum for the existence of irreversible limit cycles. We improve the quality of image tracking and disentangle the simplest mode of sperm movement - that is the planar one - with the following technique: each observed sperm has its head trapped in a microcage printed by 2-photon microlithography, see Fig. 1d and Appendix A. The cell cannot spin and the flagellum beats on the  $\hat{x}\hat{y}$  plane. While the most common swimming strategy of sperm cells is helical [9, 36], planar movement is typically observed close to a surface and can lead to circular paths [37–39], here prevented by the cage. The sperm’s center of mass has a very limited dynamics in the  $\hat{x}\hat{z}$  plane but can oscillate along the transverse  $\hat{y}$  direction; the body, entirely free, performs planar tail beating which pushes the body into the cage making the escape probability negligible. As a direct consequence of tail beating, the head is also observed to oscillate: our main results are obtained by tail tracking, while in the Supplementary Information we confirm our conclusions by tracking the head.

Referring to Fig. 1d, our region of interest (ROI) tracks less than half of the observed beating wavelength. After image processing (see Appendix B) each tail’s image is fitted through a second order polynomial  $y(x, t) = a(t) + b(t)x + c(t)x^2$  (see also Movie in the Supplementary Information). Under the assumption that the ROI contains less than half wavelength (and therefore  $y(x, t)$  has at most one extremal point),  $a(t)$  and  $b(t)$  are - but for multiplicative constants - fair approximations of the coefficients  $A(t)$  and  $B(t)$ , respectively, of a mode expansion

$$y(x, t) \approx A(t) \cos(kx) + B(t) \sin(kx) \sim_{x \rightarrow 0} A(t) + kB(t)x + \mathcal{O}(x^2) \quad (3)$$

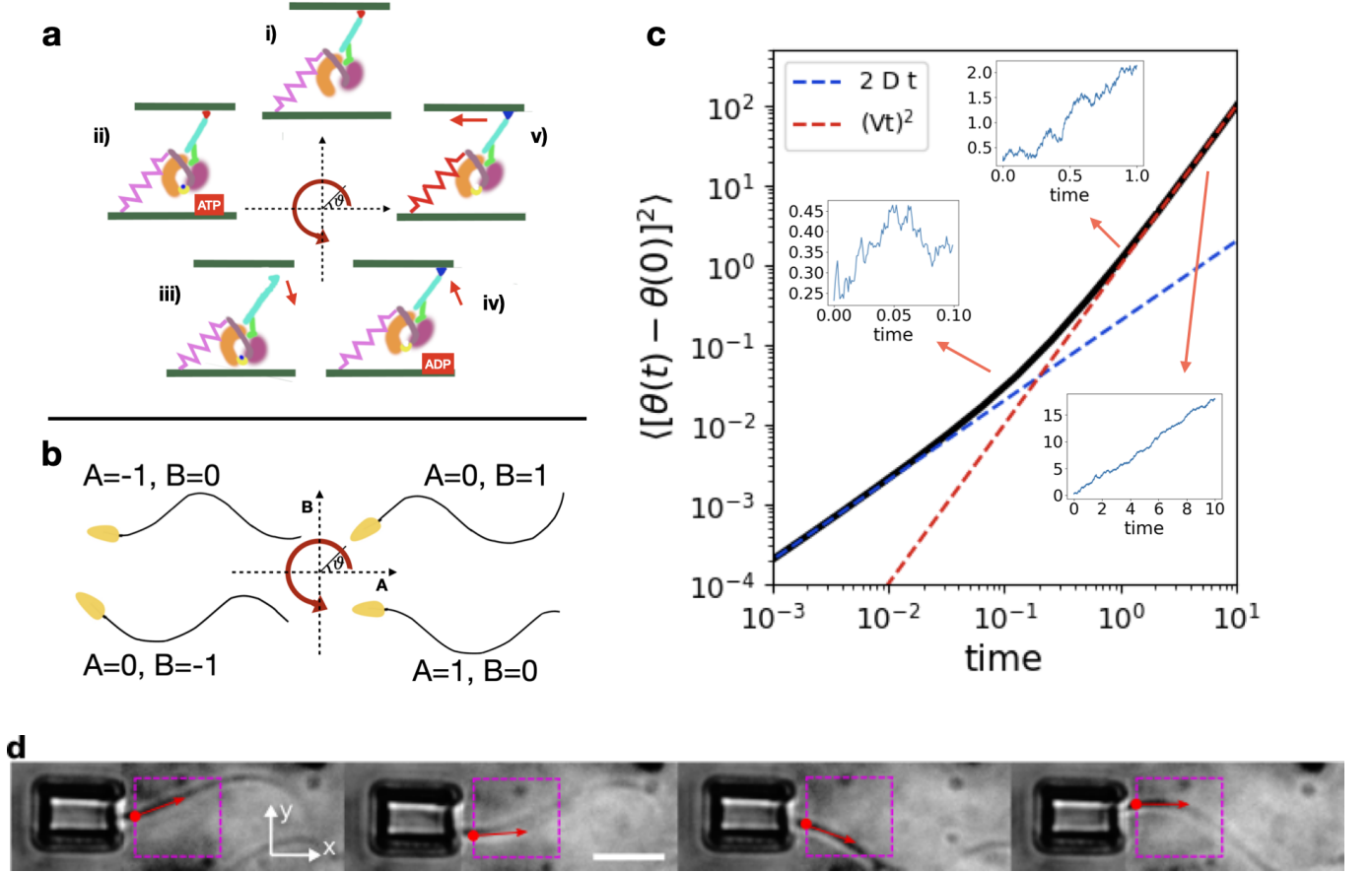


FIG. 1: Precision of stochastic clocks. Examples - in different systems - of the coarse-grained coordinate  $\theta(t)$  useful to define the precision  $p$  of Brownian clocks. **a**, Sketch of the supposed chemical cycle of the dynein ATP-ase, anti-clockwise starting from the top: i) “rest” (apo) state, ii) ATP-binding; iii) detachment of the stalk; iv) ATP  $\rightarrow$  ADP+P reaction with re-joining of the stalk to the upper substrate, in a forward position; v) stroke of the linker (red spring) with consequent dragging of the upper substrate. **b**, Sketch of the elasto-mechanical cycle of a sperm cell, the tail shape is approximated by a curve close to  $A(t) \cos(kx) + B(t) \sin(kx)$ . **c**, Mean squared displacement from a trajectory generated by the numerical integration of equation  $\dot{\theta} = V + \sqrt{2D}\eta(t)$  with  $\eta(t)$  white noise with unitary amplitude, with  $V = 1$  and  $D = 0.1$ . The insets show the trajectory  $\theta(t)$  with a different time-range, i.e. c1)  $t \in [0, 0.1]$ , c2)  $t \in [0, 1]$ , c3)  $t \in [0, 10]$ . It is evident how the mean current  $\bar{\theta} = V$  can be appreciated only at times much larger than  $1/p = D/V^2$ . **d**, successive snapshots (taken at a distance 0.04 seconds with an optical microscope, see Appendix A) of the tail dynamical sequence in a caged sperm experiment: the purple box represents the region of interest, the red dot and red arrow identify the parameters  $a, b$  (y-position and slope of the tail close to the origin, respectively) which approximate  $A, B$  in Eq. (3), here corresponding to  $(A, B) \sim (0, 1) \rightarrow (-1, 0) \rightarrow (0, -1) \rightarrow (1, 0)$ . The white arrows indicate  $\hat{x}$  and  $\hat{y}$  directions ( $\hat{z}$  direction is perpendicular to both). The white scalebar represents  $10\mu\text{m}$ .

Such a kind of shape approximation and the consequent coarse-graining of the planar flagellum dynamics into two main coordinates  $A, B$  has been used for bull sperms [20], with *Chlamydomonas* flagella [15–19] and with human sperms [39]. A similar approach to the breakdown of detailed balance in flagella has been adopted in experiments with *Chlamydomonas* [40], with filaments in actin-myosin networks [41], with *C. elegans* worms [42]. A general perspective about this strategy is discussed in a recent review [43]. In experiments of this kind, however, precision

and TUR are rarely considered [44, 45].

For the purpose of estimating  $p$  for each cell, we first apply a filter to the  $a(t), b(t)$  time series in order to remove low-frequency drifts, including average, and normalise the data to have a standard deviation of 1. We observe that the two coordinates exhibit almost harmonic oscillations at a similar frequency  $f \sim 6 - 8\text{Hz}$  (see spectra in Appendix B, Fig. 6b,c) but with a phase delay  $\Delta(t)$  that fluctuates around a steady non-zero value (Fig. 6a). This delay allows us to reconstruct the angle  $\theta(t)$  in the

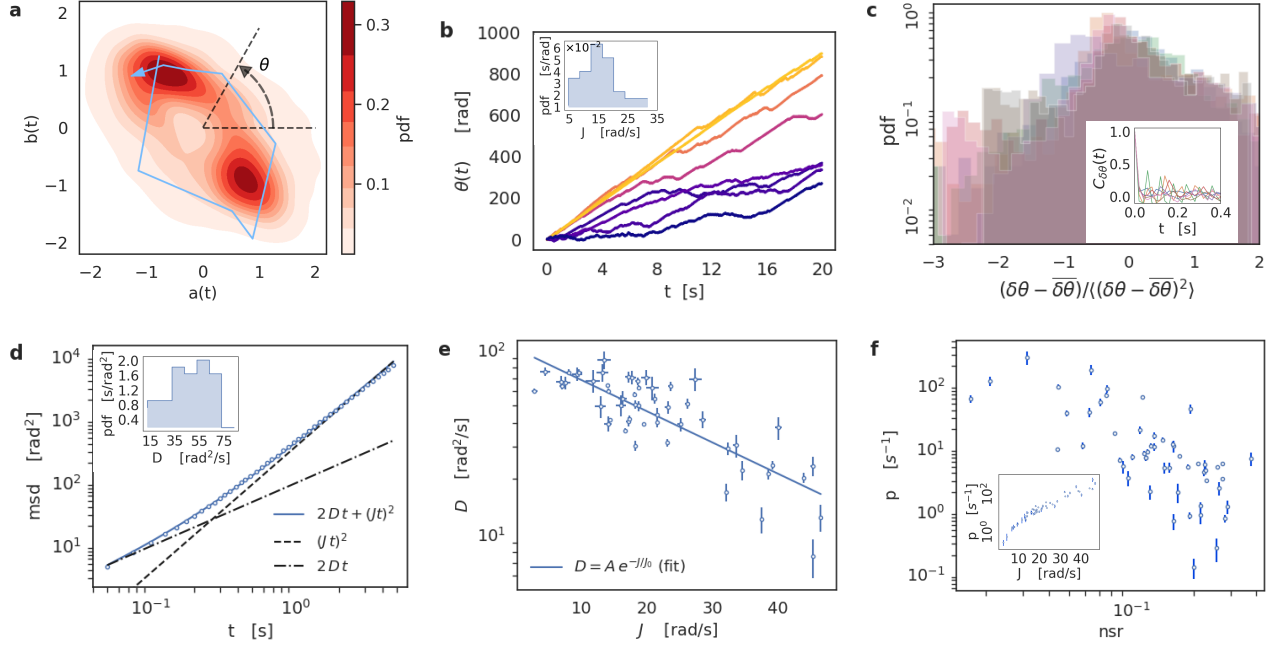


FIG. 2: Extracting precision from tail tracking. **a**, Histogram of the positions in the plane  $a(t), b(t)$  for the 12 sperms with precision  $p > 20s^{-1}$ . The light-blue curve traces the  $a(t), b(t)$  path for a particular sperm in 0.2 seconds (10 frames). **b**, Integrated phase-space current  $\theta(t)$  for a few observed sperms. The inset shows the probability density (pdf, over all observed sperms) of the average current  $J$ . **c**, Pdf (over 20 seconds acquisition), for a few sperms, of  $\delta\theta = \theta(t + dt) - \theta(t)$  (shifted by the mean and scaled by the standard deviation), where  $dt = 0.02$  seconds. The inset shows a few autocorrelations  $C_\theta(t) = \langle \delta\theta(t)\delta\theta(0) \rangle$  where  $\delta\theta = \delta\theta - \langle \delta\theta \rangle$ . **d**, Mean squared displacement of  $\theta(t)$  for a given sperm, and its fit according to the model  $msd(t) = 2Dt + (Jt)^2$ . The inset shows the pdf of diffusivity  $D$  over all observed sperms. **e**, Diffusivity  $D$  versus average current  $J$  together with decaying exponential fit  $D \sim 10^2 * e^{-J/25} s^{-1}$ . **f**, Precision  $p$  versus the noise-to-signal ratio (nsr) computed from the signals  $a(t)$  and  $b(t)$ . The inset shows the  $p$  versus the current  $J$ . Errorbars for  $J$  and  $D$  (in plots e and f) denote 3 times the stdev of  $J$  and  $D$  estimated when fitting the msd by chi-square optimization. Data come from the observation of 54 different sperm cells, if not differently specified.

plane  $a(t), b(t)$ , see Fig. 2a, and finally measure the average phase-space current  $J = \langle \dot{\theta}(t) \rangle / t$ , see Fig. 2b. Apart from a few noise dominated cells where  $J$  is small and negative we find  $J > 0$ , as expected from the geometrical interpretation of  $a(t)$  and  $b(t)$  in terms of the main modes of the tail's shape. A negative  $J$  would correspond to a waveform travelling in a direction that is incompatible with forward swimming. We stress that the cumulated phase-space angle  $\theta(t)$  is proportional to the number of performed cycles of the sperm's tail shape dynamics. The average current  $|J|$  is related to the beating frequency  $f$  in a subtle way: in fact, the growth of  $\theta(t)$  is influenced not only by the oscillation of  $a(t)$  and  $b(t)$  but also by the sign of their phase delay  $\Delta$ . Failures to guarantee a constant sign of  $\Delta$  imply *ineffective beatings*, i.e. uncoordinated oscillations which do not contribute to the growth of  $\theta(t)$ , leading to  $|J| \leq J_{max} = 2\pi f$ .

Fluctuations of the rotation speed  $\dot{\theta}(t) - J$  are well visible in our experiment, see Figs. 2b and c, and represent departures from the average shape cycle  $\theta_{ideal}(t) = Jt$ . They are in part due to real dynamical noise (“stochastic deviations”) and in part to the fact that the real shape dynamics is slightly different from the approximated one

(“deterministic deviations”). Since deterministic deviations are periodic and each experiment includes hundreds of beating periods, their contribution to the diffusivity  $D$  can be safely neglected for our purpose. The main origin of stochastic deviations is non-equilibrium fluctuations, acting both on the fluid surrounding the flagellum and on the working cycle of the thousands of molecular motors actuating the flagellum. At low Reynolds numbers the first effect is negligible (see Appendix B.2).

We empirically find a good fitting model for the mean squared displacement ( $msd$ )  $\langle [\theta(t + \tau) - \theta(t)]^2 \rangle \sim J\tau + 2D\tau^2$  (averaged over  $t$  along each whole experiment), see Fig. 2d for an example. Alternative ways to estimate the diffusivity are discussed in [20], we have considered them for our experiment, finding a substantial agreement, see the Supplementary Information. In Fig. 2e we show the relation between diffusivity  $D$  and average current  $J$  displaying an average decay but with strong fluctuations. In Fig. 2f we plot the measured values of  $p$  in a large set of experiments, as function of the noise-to-signal ratio (defined as the ratio between the peak of the spectrum and its average at frequencies higher than the oscillation frequency, see Fig. 6 in the Appendix B), and - in the inset -

versus  $J$ . Our first main conclusion is that  $p$  takes values in the approximate range  $0 - p_{max}$  with  $p_{max} \approx 10^2 s^{-1}$ . Moreover we see that it roughly decreases with the noise-to-signal ratio and it roughly increases with  $J$ . A visual inspection of the extremal cases, i.e. those close to 0 and those close to  $p_{max}$ , confirm that they correspond to chaotic motion and to almost regular periodic motion respectively.

#### 4. THERMODYNAMICS BOUNDS SPERM PRECISION

Direct empirical estimates of the energy consumption - through respiration and glycolysis - for various types of sperms, gave figures in the range of  $10^7 \div 10^8 k_B T/s$ , see Appendix B [27, 46, 47]. Theoretical estimates for the power produced by a micro-swimmers are given by the Taylor formula, here adapted for bull sperms [47]:

$$\dot{W}_{prod} \approx \pi^3 \eta L f^2 \beta^2, \quad (4)$$

where  $\beta$  is the tail beating amplitude,  $L$  is the tail length and  $\eta$  the host fluid viscosity (we have assumed, in the original Taylor's formula, the cross section of the flagellum to be  $\sim 0.2 \mu m$  and the tail wavelength  $\sim 35 \mu m$ ). We set  $\beta = 5 \mu m$  (only weakly varying with external conditions in our range, see [48]),  $L = 60 \mu m$ ,  $\eta = 10^{-3} Pa \cdot s$ . The accepted order of magnitude of sperm's efficiency is  $\sim 10 - 25\%$  [49–54], giving values which are compatible with experimental estimates  $\dot{W} \approx 10^8 k_B T/s$  when  $f = 20 Hz$  at  $37^\circ C$ . In our experiments at room temperature  $\sim 20^\circ C$  the typical beating frequency is  $6 - 7 Hz$ , leading to  $\dot{W} \approx 10^7 k_B T/s$ , and therefore  $p_{TUR} = 10^7 s^{-1}$ . It is clear that all these figures rest in a much narrower range if the normalised consumption rate is considered  $\dot{W}/f^2 \approx 2 - 5 \cdot 10^6 k_B T s$ . In conclusion the bound Eq. (2) largely overestimates our measured maximum precision, with  $Q_{macro} = p_{max}/p_{TUR} \sim 10^{-5}$ . In the following we propose an interpretation of this result.

An intriguing observation concerns the maximum precision, computed from empirical data-informed models, of the dynein molecular motors  $p_d$  [34] which is close to the maximum values we have measured for the whole flagellum  $p_d \sim p_{max}$  [67]. Our interpretation of the similarity between those two figures is the following. Let us denote with  $\theta_i(t)$  the integrated current - in the space of motor configurations - in the time  $t$  for the  $i$ -th dynein motor. In both the systems (sperm's flagellum and dynein) the current integrated in time counts the cumulated number of performed cycles in the configuration space. We conjecture that - in a given amount of time - the number of cycles in the configuration space of the sperm's flagellum is proportional to the number of cycles in the motor configuration space of *any* molecular motor in that flagellum, i.e.  $\theta(t) \approx C \theta_i(t)$ ,  $\forall i \in [1, N]$ , with possible  $i$ -dependent corrections which rapidly vanish with  $t$ . The result of this conjecture is that the precision of variable  $\theta(t)$  is close to the precision of variables  $\theta_i(t)$  for any  $i$ . The biological

meaning of our conjecture is that a long-range coordination among molecular motors inside the flagellum, quite an accepted fact in the literature [30], affects also fluctuations. In order to make our conjecture more robust, we proceed along two different roads: an experimental and a theoretical one.

Experimentally, we reconsider the TUR, Eq. (2). For a single dynein motor, in fact, it establishes a *close* upper bound:  $Q_{micro} = p_d/(\dot{W}_{dynein}/k_B T) \gtrsim 10^{-1}$ . The closeness of the bound suggests that a variation of energy consumption must reflect into a proportional variation of dynein's precision, confirmed also in theoretical models [34]. Therefore, if the noise of the flagellum beating is dominated by molecular motors' noise, a reduction of energy consumption should reflect into a reduction of the flagellum's  $p_{max}$ .

We have performed a series of experiments in oxygen deprivation, see Fig. 3. The samples were let in a sealed box for several hours, recording activity and assessing the  $p$  of all trapped cells, every 15 – 30 minutes. During the total time of the experiment (5 hours) we observed a clear decay in the beating frequency  $f$ , see Fig. 3a. Although we cannot directly control if the reduction of beating frequency is induced only by the reduction of oxygen or of other nutrients, sperms clearly reduce their activity and - as a consequence - their energy consumption. During the experiment we also observed a decay of both  $D$  and  $J$  (see Fig. 3b) and most importantly of the maximum precision  $p_{max}$  by more than a order of magnitude, see Fig. 3c. Remarkably the observed decay of  $p_{max}$  is well reproduced by the decay of energy consumption *normalised* by  $N$ , i.e.  $p_{max} \approx \dot{W}/(N k_B T)$ , where  $N = 10^5$  is an estimate of the number of dynein motor domains in a flagellum [26–28], see blue solid and dashed lines in the inset of Fig. 3c. We interpret this result as an argument in favour of the conjecture that fluctuations in the flagellum beating are dominated by fluctuations of spatially correlated dynein motors. We underline that, in order to extrapolate it to other systems and more general conditions, our conclusion should not be taken literally.

A reasonable generalisation is  $p_{max} \approx \dot{W}/(\mathcal{L}_{TUR} k_B T)$  where  $\mathcal{L}_{TUR} \sim N$  is a correlation length (measured in adimensional units, i.e. as an estimate of the number of adjacent correlated motors). In the Appendix B.3 section we show that such a generalisation follows by considering a chain of molecular motors whose dynamics is correlated up to an extension of  $\sim \mathcal{L}_{TUR}$  adjacent motors, leading to a renormalisation of the precision by a factor  $\mathcal{L}_{TUR}$ . In order to corroborate our conjecture, we reconsidered several previous results where the quality factor for fluctuations was measured in different conditions and with different flagella (from sperms and *C. reinhardtii* algae) [16–20]. A summary of our and previous results is given in Table I, in Appendix B.4. Our conjecture allows to collapse new and old data upon a master curve  $\mathcal{L}_{TUR} \sim N$ , fully consistent with our hypothesis, see Fig. 4.

A last clue in support of our conjecture comes from

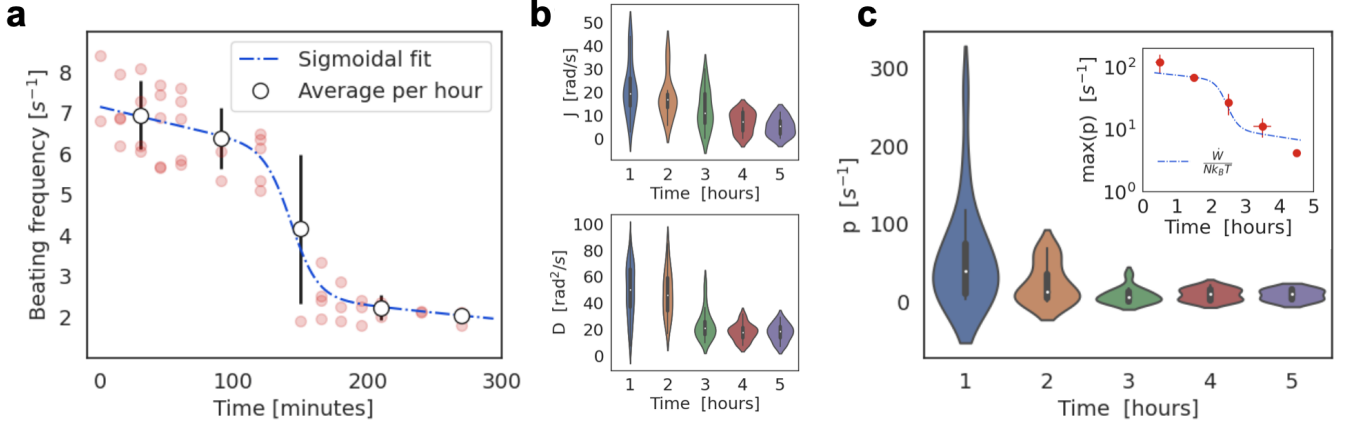


FIG. 3: Sperm precision and thermodynamics. Observations for caged sperms in experiments within a sealed chamber. **a**, Decay of beating frequency (as measured from the spectrum peak of  $a(t)$  and  $b(t)$ ), with time. The averages values of the frequencies at each hour of experiment are also marked as white circles, together with a sigmoid-like fit  $f(t) = c_1 e^{-c_2 t} s(t) + c_3 e^{-c_4 t} [1 - s(t)]$  with sigmoid  $s(t) = [1 + e^{-(t-t_0)/\tau}]^{-1}$  and best fit values  $t_0 = 143$ ,  $\tau = 10.2$ ,  $c_1 = 7.1$ ,  $c_2 = 1.1 \times 10^{-3}$ ,  $c_3 = 3.5$ ,  $c_4 = 2 \times 10^{-3}$ . **b**, reduction of average current and diffusivity along time, shown as violin plots each from a hour bin (e.g. 1 means all observation done in the 1st hour, etc.). **c**, decay of precision with time, again in the form of a violin plot. The inset shows the decay of  $p_{max}$  (estimated as the average of the top 25% population) together with the normalised (by  $N = 10^5$ ) power consumption extracted by the Taylor formula, eq. (4) using the frequency decay fit shown in Fig. 3a, with amplitude fixed at the average observed value  $5.2 \mu m$ . Errorbars represent standard deviations normalised by square root of the number of data in the aforementioned percentile. The sizes of samples in the plots of frames b and c are: 41 sperms in the 1st hour, 24 in the 2nd hour, 34 in the 3rd hour, 25 in the 4th hour and 16 in the 5th hour.

the numerical analysis of a theoretical model for the motor-actuated flagellar dynamics, extensively studied in [12, 55, 56], modified here through the introduction of a coupling term between adjacent motors. The model is schematized in Fig. 5a and is described in details in the Appendix C. It consists of a filament with  $N$  motors. Each motor acts on the filament through an interaction potential, and performs a stochastic attachment/detachment dynamics which breaks detailed balance as if consuming ATP. The motor position  $X$  oscillates under the joint effect of the forces of the attached motors and of an external elastic force  $\xi \dot{X}(t) = -\partial_X \sum_i s_i U[x_i - X(t)] - \kappa X$  with  $s_i \in \{0, 1\}$  representing the detached-attached status of  $i$ -th motor, the motor-filament potential  $U(x) = U_0[1 - \cos(2\pi x/\ell)]$ , viscosity  $\xi$  and elastic constant of the external spring  $\kappa$ . The elastic force here could represent the effect of the cage but in previous studies was introduced just to simplify the mathematics of the problem, it is not crucial for the model's phenomenology [55]. The variables  $s_i$  jump from 0 to 1 and back according to a Poisson process. In the original model the probability rates of such a process depended only upon the local motor-filament potential, so that the fluctuations of the jump dynamics of each motor was independent from nearby motors: for this reason the amplitude of the macroscopic noise was observed to decrease with  $N$  [20]. Here we employ a binding potential  $K(s_i - s_{i+1})^2$  that correlates the states  $s_i$  and  $s_{i+1}$  of adjacent motors. Increasing  $K$  (from the case  $K = 0$  which corresponds to the original version) dras-

tically changes the behavior of the model, in particular resulting in a much stronger macroscopic noise, i.e. a largely faster decay of the phase correlation, see Fig. 7 in the Appendix C. The noise reduction due to the growth of  $N$  disappears at large  $K$ . In Fig. 5b we draw our main conclusion, measuring the precision  $p = \omega^2/D$  where  $\omega$  is the average oscillation frequency and  $D$  the diffusivity deduced from the decay of phase correlation [20]. It is seen that when  $K$  increases the size-scaling of precision goes from  $p \sim O(N)$  to  $p \sim O(1)$ . This result amounts to say that the precision of the whole flagellum becomes comparable to the precision of the single motor when  $K$  is large enough. On the other side, the energy consumption (ATP consumed per cycle and per motor) increases with  $N$ , mostly independently of the coupling strength. The ratio between precision  $p \sim O(1)$  and energy consumption  $\dot{W} \sim N$  therefore decreases as  $1/N$ , in fair agreement with our experimental observations.

## 5. CONCLUSIONS AND OUTLOOK

We have reported an experimental protocol to estimate the statistical precision of sperm's beating, which differs from previous measurements of the quality factor as it is directly related to energy consumption, according to the recently celebrated TURs. The use of single-cell traps aids the reconstruction of the dynamics of a single cell's shape, but in future implementations it could be replaced by a comoving tracking analysis directly applied



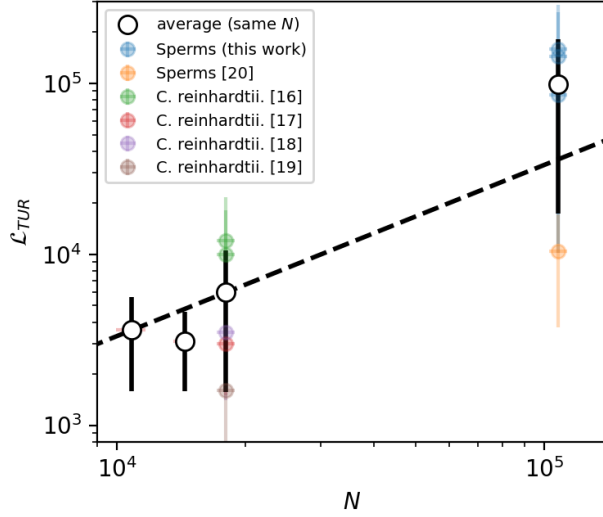


FIG. 4: Collapse of correlation lengths in several experiments. The data from different previous experiments with sperms and flagella of *C. reinhardtii* algae are summarised here by plotting the correlation length  $\mathcal{L}_{TUR} = \frac{\dot{W}}{pk_B T}$ , discussed in the Appendix B.3, versus the length of the flagella  $N$  (both quantities are given as numbers of molecular motors). The data are also reported in Table I. The light colored points allow to distinguish the different experiments, while the solid circles identify the averages at each given flagellar length. Bars represent statistical errors. The dashed line marks the scaling law  $\mathcal{L}_{TUR} \sim N$  which is expected under the hypothesis of strong coordination among adjacent motors in the axoneme.

upon free swimming cells. Future investigation should focus upon the biological relevance of the parameter  $p$ : we suggest that it influences the response of sperm cells to changes in boundary conditions, external flows, chemical gradients, etc., determining its swimming performance in complex environments.

In addition to introducing a new observable of potential biological and biomedical interest, our results point to the need of understanding dynamical fluctuations of active flagella and their relation to their bioenergetics [57–59]. It seems that a recognised theoretical statement, the Thermodynamic Uncertainty Relation, has a relevance not only for molecular motors, but also for meso-scopic self-propelling microswimmers. With this aim, we have reported two striking observations: 1) the coincidence between the maximum precision of the whole sperm cell and that of molecular motors actuating the sperm’s flagellum, 2) the dependence of the maximum precision of the whole sperm cell upon the reduction of energy consumption, a dependence that one would expect only for the molecular motors. As a common explanation we conjecture that the  $N \approx 10^5$  dynein motors actuating a sperm’s tail work at a high level of coordination which also affects fluctuations: a theoretical model where adjacent motors are coupled by a binding

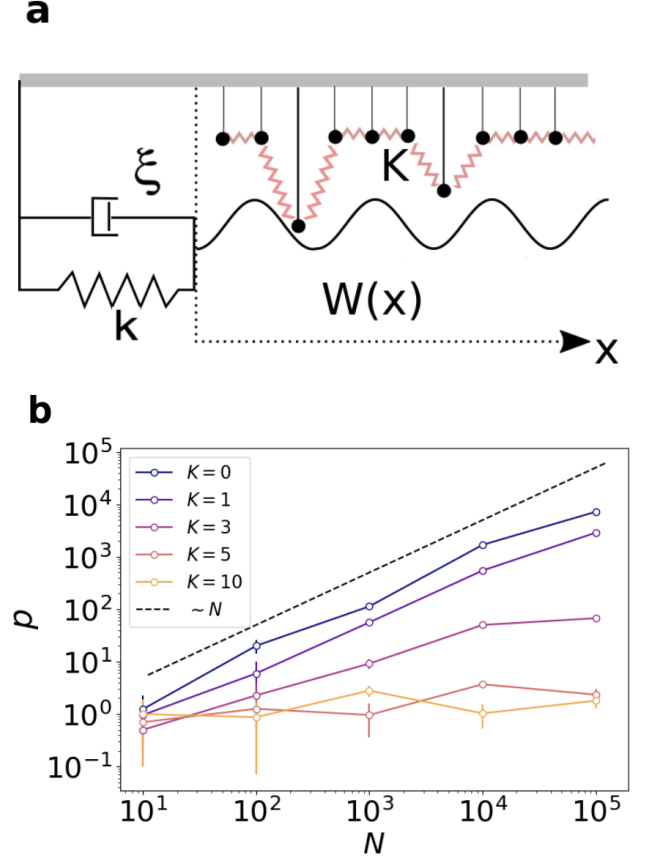


FIG. 5: Theoretical model. **a**, sketch of the model; **b**, precision  $p$  versus number of motors  $N$  for different choices of the coupling parameter  $K$ , showing the  $O(N)$  scaling for uncoupled motors ( $K = 0$ ) and the  $O(1)$  scaling for large  $K$ . In all the simulations we have used  $\alpha = \eta = 0.5$ ,  $k/(\xi\Omega) = 10$ ,  $\alpha NU_0/(\Omega\ell^2\xi) = 0.6$ . The error bars are obtained to error propagation based upon the error in the measurement of  $D$ . Such error is the estimated standard deviations of  $D$  in the non-linear least squares fit of the exponential decay of the phase correlation (see Appendix C).

potential is consistent with our observations. The TUR is therefore still valid for the whole sperm’s cell, but with a discrepancy between maximum precision and energy consumption which is  $\sim N$  times worse than in the case of the single molecular motor. An interesting perspective involves studying the same observables with other microswimmers, such as *E. coli*, whose flagellar motor fluctuations have been studied in the past [60] but not their connection with the TUR.

### Acknowledgments

A. P. and B. N. acknowledges the financial support of Regione Lazio through the Grant “Progetti Gruppi di Ricerca” N. 85-2017-15257 and from the MIUR PRIN 2017 project 201798CZLJ.

## Appendix A: Experimental

### Microfabrication

The micro-cage features allowed to accommodate one single cell on it, in a way that the head is confined while leaving the entire tail outside. Based on sperm characteristics, the chamber is designed as a box composed by four microfabricated facets anchored to the cover glass. The height, width and depth of a single cage are  $500\text{ nm}$ ,  $5.5\text{ }\mu\text{m}$  and  $11\text{ }\mu\text{m}$ , respectively. Microfabrication was carried out by a custom built two-photon polymerization setup [61]. The micro-chambers were generated from SU-8 3025 photoresist (Kayaku Advanced Materials) using a  $60\times 1.4\text{NA}$  objective. After exposure, the photoresist sample was baked ramping the temperature from  $65\text{ }^\circ\text{C}$  up to  $95\text{ }^\circ\text{C}$  with increments of  $5\text{ }^\circ\text{C}$  per min, then 7 min at the highest temperature. Reduction of stress between the substrate and SU-8 is achieved by gradually decreasing the temperature of the sample until reaching room temperature. Thereafter, the photoresist was developed by its standard developer solvent, followed by rinsing in a 1:1 solution of water and ethanol, and finally dried with a gentle blow of nitrogen. Strong adhesion of the micro-chambers to the carrier cover glass was ensured by three layers of Omnicoat adhesion promoter (Kayaku Advanced Materials). Laser power and scanning speed were  $5\text{ mW}$  and  $30\text{ }\mu\text{ms}^{-1}$ , respectively.

### Sample preparation

The experiments for measuring the main spatial modes of the sperm's tail were developed on an open sample. This sample was obtained by attaching a plastic ring surrounding the micro-chambers area using the optical adhesive NOA81 (Norland Products Inc.). For the experiments under oxygen deprivation we used hermetically sealed samples. Two fishing wires of  $\sim 100\text{ }\mu\text{m}$  thickness and NOA81 adhesive were used as spacers between the carrier cover glass and a cover slip, generating a channel; after introducing approximately  $150\text{ }\mu\text{L}$  of solution containing sperm cells, the sample was completely sealed by applying NOA81 adhesive in the two open sides. Bull sperms were obtained from "Agrilinea S.R.L." (Rome), and stored in a liquid nitrogen cylinder. On the day of the experiment, a vial of sperms suspended in semen was taken and immersed in a hot water bath of  $37\text{ degrees centigrade}$  for 10 minutes. The vial was then taken out of the bath and immediately cut open using a pair of sterilized scissors. The sperm suspension was poured out of the vial in an Eppendorf. A micropipette was then used to suck out  $150\text{ }\mu\text{L}$  of the sperm suspension from the Eppendorf and insert the fluid into the microchannel, ensuring proper filling inside the structures. The sperm movement was recorded at environmental temperature,  $\sim 20^\circ\text{C}$ , by using a digital camera (Nikon, USA) connected to an inverted microscope. The image capturing

and analysis was performed using an in house software made using Python Programming language

## Appendix B: Data Analysis

### Details about the tail-tracking procedure

Images are collected at 50 frames per second, with  $20\times$  objective resulting in a resolution of  $6.5/20\text{ }\mu\text{m}$  per pixel. Each image portrays a large portion of the substrate where several cages are present, almost all filled by caged sperms. Only cages with a single trapped sperm cell are analysed. A region of interest (ROI) of averagely  $40\times 40$  pixels - corresponding to an area of roughly  $13\times 13\text{ }\mu\text{m}^2$  - containing the most visibile part of the tail which is also the one closest to the head (see Fig. 1d), is cropped and treated by successive layers of image processing tools: 1) background subtraction to reduce noise, 2) transform to gradient (squared modulus) to avoid dependence on absolute levels, 3) gaussian filter with 1 pixel range, 4) the largest continuous bright region is individuated (it always corresponds to the tail), 5) that region is treated as a cloud of scattered points representing a curve  $y$  vs.  $x$ , which is fitted by least squares to a second order polynomial  $y(x,t) = a(t) + b(t)x + c(t)x^2$  as discussed in the main text. The time series of  $a(t)$  and  $b(t)$  are filtered by a 3rd order Butterworth high-pass digital filter with critical frequency set  $1.5\text{ Hz}$ . In Figure 6 the time series of  $a(t)$  and  $b(t)$  of a tracked cell are shown, together with the spectra of the two series before and after the filtering. The noise-to-signal ratio (nsr) is computed as the ratio between the noise level and the signal level, both shown in the Figure.

### Discussion of thermal diffusion effects due to the fluid

The value of  $D$  is the result of a complex interplay of elasticity, hydrodynamics, activity and noises with different origins. Even at thermal equilibrium, i.e. for dead sperms, an estimate of filament phase diffusivity is complex as it involves not only the amplitude of fluctuations, that can be inferred by equilibrium distribution of elastic energy, but also the relaxation time of such modes. A first estimate of involved timescales can be obtained by computing the rotational diffusivity. For a passive rod [62] (or a filament with low flexibility) of length  $\ell \approx 50\text{ }\mu\text{m}$  (as the sperm's body) in water viscosity  $\eta$  one has a rotational diffusivity of the order  $D_{Stokes} \approx k_B T / (\eta \ell^3) \approx 10^{-5} \text{ rad}^2/\text{s}$ . Visual inspection of our samples show that non-motile cells are basically immobile with negligible fluctuations in position or in shape, within our space-time resolution.



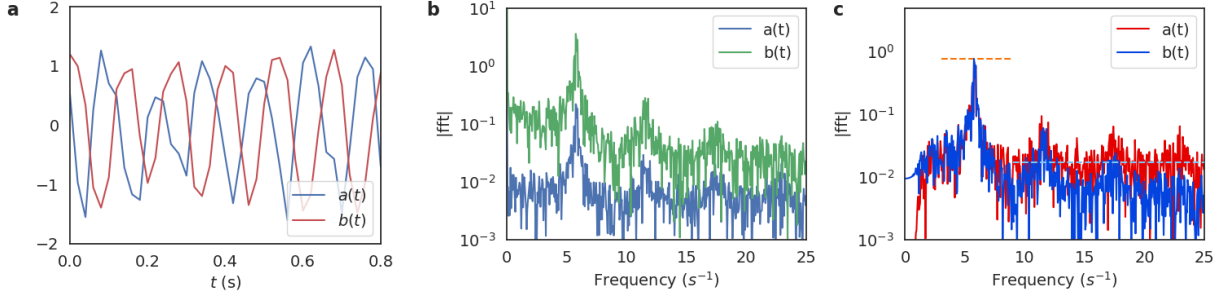


FIG. 6: Details about the tail-tracking procedure. **a**, Examples of the signals  $a(t)$  and  $b(t)$  from trail tracking: one can see that  $a(t)$  anticipates  $b(t)$  of an angle between  $\sim \pi/2$  and  $\sim \pi$ . **b**, spectra (modulus of the fast Fourier transform) of the signals  $a(t)$  and  $b(t)$ . **c**, spectra after signal filtering. The orange and light-blue dashed lines indicate the signal level and the noise level respectively (the noise-to-signal ratio  $\text{nsr}$  is defined as the ratio between the latter and the former).

### Correlation length based upon the thermodynamic uncertainty relation

Here we discuss a simple scaling argument to pinpoint the minimal assumptions behind the definition of an uncertainty correlation length

$$\mathcal{L}_{TUR} = \frac{\dot{W}}{p_N k_B T} \quad (5)$$

for a system of  $N$  connected motors (e.g. a chain similar to the axoneme structure). We recall that the asymptotic (steady state) precision  $p$  is defined as

$$p_N = \lim_{t \rightarrow \infty} \frac{1}{t} \frac{\langle X_N(t) \rangle^2}{\langle X_N^2 \rangle_c} \quad (6)$$

where  $\langle x^2 \rangle_c$  stands for the variance of variable  $x$ , and  $X_N(t) = \int_0^t ds \dot{X}_N(s)$  is the observed integrated current.

At a first order approximation, the presence of spatial correlations across a correlation length  $\tilde{N}$  inside the chain can be accounted for by re-grouping the  $N$  motors in  $M = N/\tilde{N}$  independent groups. Moreover the observed integrated current  $X_N$  can be assumed to be an empirical average of the integrated current in each of the  $M$  independent groups, i.e.

$$X_N = \frac{\sum_{i=1}^M X_{\tilde{N},i}}{M}, \quad (7)$$

with the  $X_{\tilde{N},i}$  being independent and identically distributed. These assumptions lead to

$$p_N = \lim_{t \rightarrow \infty} \frac{1}{t} \frac{\langle X_{\tilde{N}}(t) \rangle^2}{\langle X_{\tilde{N}}^2 \rangle_c / M} = M p_{\tilde{N}}. \quad (8)$$

Assuming that the mean consumed work is extensive in the size of the chain, i.e.  $\dot{W}_N \sim N \dot{W}_1$ , we get

$$\frac{\dot{W}_N}{p_N k_B T} = \tilde{N} \frac{\dot{W}_1}{p_{\tilde{N}}} = (\mathcal{Q}_{micro})^{-1} \tilde{N}, \quad (9)$$

having considered

$$\frac{\dot{W}_1}{p_{\tilde{N}}} \approx \frac{\dot{W}_1}{p_1} = (\mathcal{Q}_{micro})^{-1} \quad (10)$$

In the last passage we have assumed  $p_{\tilde{N}} \approx p_1$  following the assumption that for the correlated  $\tilde{N}$  motors in a group the precision is that of a single motor. Eq. (9) justifies our definition in Eq. (5)

### Previous experiments with sperms at physiological temperature and with other flagella.

In a recent work [20] data from sperm cells observed at 37 °C have been analysed. Such data, collected in a previous work [63] concern an anomalous swimming regime which is apparently induced by a particular sample preparation: they were “incubated with 1% F-127 (Sigma) in PBS for 5 min.... When the surface was treated with F-127, the sperm did not stick but instead swam close to the surface, usually in circles of radii on the order of 40  $\mu\text{m}$ ” [63]. With such treatment the measured beating frequency was particularly high, we denote it as  $f_{Ma} \sim 31$  Hz, much higher than what usually observed (literature reports 20 Hz for bull sperm cells at 37 °C [48], observed also in [63] without such surface treatment). Within such particular conditions the authors measured a quality factor which, in our notation, reads  $q = J/2D \sim 38$  that would correspond to a precision  $p = 2qJ$ .

Other experimental works have addressed the properties of noise in the beating of axonemes, particularly with *Chlamydomonas* flagella [15–19]. In [16, 17] the quality factor of beating was obtained indirectly from the rate of phase slips in pairs of synchronised flagella (as well as directly from the distribution of beating periods), getting estimates in a range  $q = 25 - 120$ , with average beating frequency  $f = 50$  Hz.

A summary of such previous observations and a comparison with the results of the present study is given

in Table I. In compiling this table we have used some assumptions typically found in the literature i.e. that the amplitude of sperm's beating is  $6 \pm 1 \mu\text{m}$ , the amplitude ("wingspan") of *Chlamydomonas* flagellar beating is  $10 \pm 1 \mu\text{m}$ , and the energy consumption in both cases is given by Taylor formula Eq. (4) multiplied by 10 (that is assuming an average efficiency of 10%).

A plot of the TUR-based correlation length versus the length of the flagellum is shown in Figure 4. Within the error, the data are compatible with long-range order, i.e.  $\mathcal{L}_{TUR} \sim N$ .

### Estimates of the energy consumption and efficiency of sperm swimming.

Consumption rate, speed and beating frequency are sensitive to environmental conditions, e.g. temperature and fluid viscosity [48]. In [46] sea urchin sperm was studied in a 50% glycerol solution at  $16^\circ\text{C}$  with varying the beating frequencies through modulation of the ATP concentration: for instance at 20 Hz it was found  $10^6$  molecules of ATP per sperm per second, corresponding to slightly more than  $\approx 10^7 k_B T$  per second. In [47] experiments were performed at  $37^\circ\text{C}$ , with bull semen diluted/washed in egg yolk with diluents, a phosphate buffer and the addition of fructose and lactate, leading to an estimate of consumption rate equal to  $\approx 10^7$  molecules of ATP per sperm per second, i.e. slightly more than  $\approx 10^8 k_B T$  per second. The evaluation of the produced work through the Taylor formula led to an estimate of the efficiency of  $\sim 20\%$ . In [27] sea urchin sperms are studied one by one in droplet solutions, at unreported temperature but with controlled conditions in both ATP concentration and buffer viscosity (both directly modulating the beating frequency), obtaining  $\sim 3 \cdot 10^6$  ATP molecules per sperm per second when the tail beats at 10 Hz.

### Appendix C: A theoretical model for the fluctuations of an active axoneme

The model discussed in this section is a variation of the classical model introduced in [12] and further studied in [55] and [56].

Interestingly the original model has been used to rationalise recent experiments on sperm swimming fluctuations [20]. In the original model however, the fluctuations of the  $N$  motors are independent, therefore the fluctuations of the filament macroscopic dynamics are somehow similar to the fluctuations of an *average* of  $N$  independent noises, therefore their squared error (or diffusivity) decreases with  $N$  and this result in a linear  $\sim N$  increase of the precision (or quality factor). We provide a simple mechanism to couple the noises of the motors and verify, in numerical simulations, that this ingredient is sufficient - at strong coupling - to change the size scaling

from  $O(N)$  to  $O(1)$ .

In the model the filament is represented by a position  $X(t)$  and by a potential  $W = \sum_{i=1}^N s_i U[x_i - X(t)]$  which regulates the interaction of the filament with  $N$  motors, each one being at fixed position  $x_i$  and in attachment state  $s_i = 0, 1$  (0 when detached and 1 when attached). The position  $X(t)$  can be understood as the real position in space of the center of mass of the filament, as well as a generalised coordinate representing the shape of it. The potential may be related to local properties of the filament, such as the local curvature which depends upon the time  $t$  through the coordinate  $X(t)$ . Each motor can detach and re-attach from/to the filament, changing its state  $s_i$ , according to a Poisson process that violates detailed balance, as it happens when  $\text{ATP} \rightarrow \text{ADP} + \text{P}$  eso-energetic process is involved. The overdamped equation of motion of the filament is  $\xi \dot{X}(t) = F_{\text{ext}}(t) + F(t)$  where  $F(t) = -\partial_X \sum_i s_i U[x_i - X(t)]$  and  $F_{\text{ext}}(t)$  is an external force. In general the filament can be free from external forces, but then a spatial asymmetry (employed in  $W(x)$ ) is needed to induce forward motion, otherwise an external force (e.g. a spring on an end of the filament) is already sufficient to break spatial symmetry and the potential  $W$  can be taken symmetric to simplify calculations. This is the case analysed here and in [20], with  $F_{\text{ext}} = -\kappa X$  and  $U(x) = U_0[1 - \cos(2\pi x/\ell)]$ , the filament does not move on average but fluctuates more or less regularly, while a limit cycle in the plane  $X(t), F(t)$  can be used as analogous to the  $A, B$  plane used in our experiments. In the original model, each motor realises the attachment/detachment process independently from the other motors, with the only indirect correlations due to the modulation of the attachment/detachment rate through the position  $\omega_{on}^i = \Omega[\eta - \alpha \cos(2\pi(x_i - X(t))/\ell)]$  and  $\omega_{off}^i = \Omega - \omega_{on}^i$ . This ingredient however only correlates (locally) the average residence times but does not correlate fluctuations around those averages: it is the same as considering independent noises with similar averages.

In order to adapt the model to our experimental findings, we introduced a binding potential that correlates adjacent motors: this potential is minimised when adjacent motors are in the same state. This is implemented as a modification of the rates according to the formula  $\omega_{on}^i = \Omega[\eta - \alpha \cos(2\pi(x_i - X(t))/\ell)]e^{-\Delta U_i^{\text{bind}}}$  and  $\omega_{off}^i = \Omega - \Omega[\eta - \alpha \cos(2\pi(x_i - X(t))/\ell)]e^{-\Delta U_i^{\text{bind}}}$ , with  $\Delta U_i^{\text{bind}}$  is the binding potential increase after the variation of state  $s_i$  of the  $i$ -th motor, and the binding potential is  $U_i^{\text{bind}} = K(s_i - s_{i+1})^2 + K(s_i - s_{i-1})^2$ . When  $K = 0$  the original model without binding energy is recovered.

The effect of  $K$  can be appreciated in numerical simulations of the model whose results are reported in Fig. 5 and 7. In particular in Figure 7c-f we show the drastic change in the decay of the phase correlation when  $K$  is increased. In Fig. 5b it can be appreciated how the size scaling of the precision changes completely and tends to become *independent* of  $N$  when the coupling strength

Experiment	$f$	$L$	$N$	$\dot{W}/(k_B T)$	$q$	$p$	$\mathcal{L}_{TUR}$
Sperms (this study)	$8 \pm 1$	$60 \pm 3$	$1.1 \cdot 10^5$	$10^7$	/	$120 \pm 30$	$8.5 \cdot 10^4$
Sperms after $\sim 2$ hours	$6 \pm 1$	$60 \pm 3$	$1.1 \cdot 10^5$	$5.7 \cdot 10^6$	/	$60 \pm 10$	$9.6 \cdot 10^4$
Sperm after $\sim 4$ hours	$3 \pm 1$	$60 \pm 3$	$1.1 \cdot 10^5$	$1.4 \cdot 10^6$	/	$10 \pm 5$	$1.4 \cdot 10^5$
Sperm after $\sim 5$ hours	$2 \pm 1$	$60 \pm 3$	$1.1 \cdot 10^5$	$6.4 \cdot 10^5$	/	$4 \pm 0.5$	$1.6 \cdot 10^5$
Sperms at 37 °C [20]	$31 \pm 1$	$60 \pm 3$	$1.1 \cdot 10^5$	$1.5 \cdot 10^8$	$38 \pm 5$	$1.4 \cdot 10^4$	$10^4$
Chlamydomonas [16]	$47 \pm 2$	$10 \pm 0.5$	$1.8 \cdot 10^4$	$1.6 \cdot 10^8$	$23 \pm 16$	$1.3 \cdot 10^4$	$1.2 \cdot 10^4$
Chlamydomonas [16]	$47 \pm 2$	$10 \pm 0.5$	$1.8 \cdot 10^4$	$1.6 \cdot 10^8$	$26 \pm 18$	$1.6 \cdot 10^4$	$10^4$
Chlamydomonas [17]	$71 \pm 2$	$6 \pm 0.5$	$10^4$	$2.3 \cdot 10^8$	$70 \pm 10$	$6.2 \cdot 10^4$	$3.6 \cdot 10^3$
Chlamydomonas [17]	$67 \pm 2$	$8 \pm 0.5$	$1.4 \cdot 10^4$	$2.6 \cdot 10^8$	$100 \pm 12$	$8.3 \cdot 10^4$	$3.1 \cdot 10^3$
Chlamydomonas [17]	$62 \pm 2$	$10 \pm 0.5$	$1.8 \cdot 10^4$	$2.9 \cdot 10^8$	$120 \pm 18$	$9.6 \cdot 10^4$	$3 \cdot 10^3$
Chlamydomonas [18]	$60 \pm 3$	$10 \pm 0.5$	$1.8 \cdot 10^4$	$2.7 \cdot 10^8$	$100 \pm 20$	$7.5 \cdot 10^4$	$3.5 \cdot 10^3$
Chlamydomonas [19]	$53 \pm 2$	$10 \pm 0.5$	$1.8 \cdot 10^4$	$2 \cdot 10^8$	$199 \pm 20$	$1.3 \cdot 10^5$	$1.6 \cdot 10^3$

TABLE I: Summary table of results from previous literature and from the present studies for both sperms and Chlamydomonas. The columns report the kind of experiment (with reference), the frequency of beating (in Hz), the length of the flagellum (in  $\mu m$ ), the estimated number of motors  $N = 1800L$ , the energy consumption in units of  $k_B T$ , the quality factor  $q$  (when measured), the maximum observed precision (or maximum precision)  $p$  (in  $s^{-1}$ ) and the precision-based correlation length  $\mathcal{L}_{TUR} = \dot{W}/(pk_B T)$  in number of motors, see Appendix B.3. For reasons of space we have not reported the errors if they can be computed by standard error propagation. The reported errors are those obtained from estimate reported in the literature and standard deviations in our experimental observations.

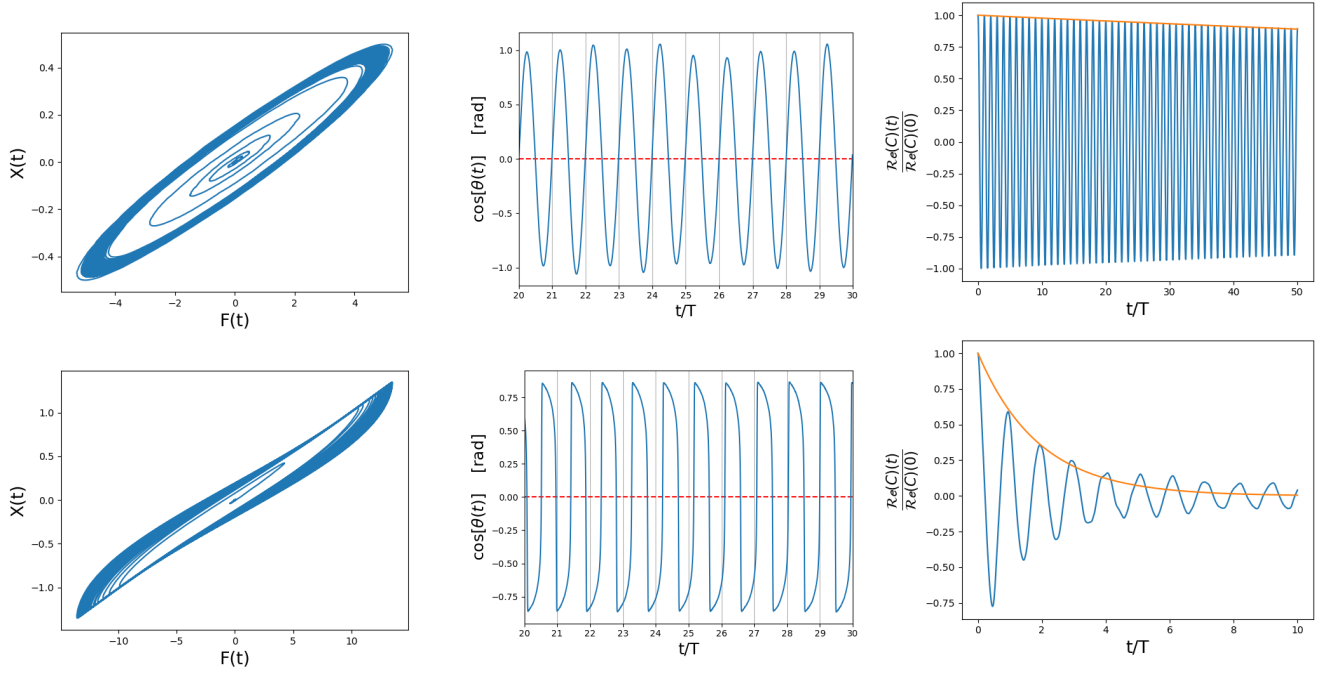


FIG. 7: Theoretical model. **a,d**, evolution of the system in the force-coordinate phase space ( $K = 0$  in **a** and  $K = 10$  in **d**), the angle  $\theta(t)$  measures the phase of this limit cycle after suitable rotation and normalisation of axis; **b,e**, evolution of  $\cos[\theta(t)]$  that allows to evaluate the stability of the periods in the two cases ( $K = 0$  in **b** and  $K = 10$  in **e**); **c,f**, real part of the autocorrelation of  $e^{i\theta(t)}$  and exponential fit  $\sim e^{-Dt}$  of its envelope ( $K = 0$  in **c** and  $K = 10$  in **f**). In all the simulations we have used  $\alpha = \eta = 0.5$ ,  $k/(\xi\Omega) = 10$ ,  $\alpha NU_0/(\Omega\ell^2\xi) = 0.6$ .

increases. Our observation that the macroscopic sperm precision ( $N \sim 10^5$ ) is similar to the microscopic sperm precision ( $N = 1$ ) is fairly explained by this new model. Note that the beating frequency in the model is independent of  $N$  (at least for  $N \gtrsim 10^2$ ) so that the energy

consumption (ATP consumed per cycle and per motor) increases with  $N$ , even for large binding potential. The ratio between precision  $p \sim O(1)$  and energy consumption  $\dot{W} \sim N$  is therefore doomed to decrease as  $1/N$ , in fair agreement with experimental observations.

## Appendix D: The simplest working principle for Thermodynamic Uncertainty Relations

While the TURs have been demonstrated for larger and larger classes of models and time domains, we judge instructive to riepilogate the first example where they have been observed which is a Markov jump process describing - in a very simplified way - the stochastic (progressive on average) dynamics of a single Brownian motor or clock [23]. The model is defined in continuous time, the motor can go forward or backward with probability rates  $k_+$  and  $k_-$  respectively. Local detailed balance dictates  $k_+/k_- \sim \exp(Q/k_B T)$  where  $Q = W$  is the energy dissipated in a forward jump equal to the work input carried by ATP.

The average current of the clock (number of steps per unit of time) is  $J = k_+ - k_-$ , while the associated diffusivity is  $2D = k_+ + k_-$ , therefore for the position  $X(t)$  of the motor/clock one has a relative uncertainty  $\epsilon^2 = (\langle X^2 \rangle - \langle X \rangle^2) / \langle X \rangle^2 = 2Dt / (Jt)^2 = (k_+ + k_-) / [(k_+ - k_-)^2 t]$  which in terms of the precision  $p = 2 / (t\epsilon^2)$  reads  $p = 2(k_+ - k_-)^2 / (k_+ + k_-)$ . The energy dissipated up to time  $t$  is  $T\sigma t = \dot{Q}t = JQt$ . Then the product between the energy dissipated and the relative uncertainty satisfies  $2\dot{Q}/p = T\sigma t\epsilon^2 = (k_+ + k_-) / (k_+ - k_-) Q \coth[Q/(2k_B T)] \geq 2k_B T$  which leads to the TUR used in this paper  $p \leq \dot{Q} / (k_B T)$ .

This example is useful to evaluate the key sources of noise in this process, i.e. the contributions to  $D$  which are both  $k_+$  and  $k_-$ . This means that backstepping (a not negligible  $k_-$ ) is not the only source of noise, but  $k_+$  also contributes to noise. The reason is that a large contribution to fluctuations of the motor current is due to fluctuations in the residence time before a new forward step. If time is discretized in  $dt$  steps, the motor remains in its position with a probability  $1 - (k_+ dt) - (k_- dt)$ : the exit time has an exponential probability with average exit rate  $(k_+) + (k_-)$ . The real chemical network of a molecular motor, such as the dynein, is much richer than the minimal model considered in [23, 64, 65]: in that minimal model a single step is a coarse-graining of the several intermediate chemical steps. The presence of intermediate steps with their fluctuating residence of times and possibly non-negligible backstepping probabilities implies relevant fluctuations in the coarse-grained residence times and therefore in the motor's current, even when the total back-stepping probability is negligible. We deem these motors' fluctuations, with an additional coordination hypothesis discussed in the text, to be important for the deviation of the sperm shape cycle from its average dynamics.

## SUPPLEMENTARY INFORMATION

### Tracking the head oscillations

In a series of experiments we have tracked the sperm's head instead of the tail, finding results in qualitative and quantitative agreement with those reported in the main article. The setup is identical, but different lighting and focus conditions with the microscope allowed us to have more image contrast in the interior of the cages. Images are collected with the same objective and ccd as in the main experiment. The region of interest is averagely the same area as in the main experiment. Background subtraction reduces the visibility of cage's boundaries. The covariance matrix of the pixel light distribution is computed: its eigenvector associated to the maximum eigenvalue determines the direction of orientation of the sperm's head, whose slope replaces coefficient  $-b(t)$  of our tail's analysis (the minus sign of course depends upon the reference frame we are using). The  $\hat{y}$  position of the center of mass of the head replaces coefficient  $a(t)$ . Once we get  $a(t), b(t)$  for the image at time  $t$  we can repeat exactly the same analysis as we did for the tail's tracking. In Figure 1 we summarise the results of this analysis.

### Alternative estimates of the precision

In a recent paper the fluctuations of the sperm beating cycle have been analysed [20]. The Authors suggest two alternative ways to estimate the phase diffusivity  $D$  which is necessary to get values for  $p = J^2/D$  (being  $J = 2\pi f$  and  $f$  the average beating frequency). A first, perhaps more approximate, procedure is to retrieve the quality factor  $q = f_0/\Delta f_0$  where  $\Delta f_0$  is the width-at-half-maximum in the power spectrum, which reads  $\Delta f_0 \sim 3$  Hz giving  $q \approx 3$ . The quality factor is related to the phase diffusivity by  $q = J/(2D)$  which leads to  $p = J^2/D = 2Jq \approx 2 \times 10^2 s^{-1}$  which is compatible in order of magnitude with the maximum precision we report in the main text. The second recipe consists in measuring the decay in time of the phase correlation  $C(t) = \langle \exp i[\theta(t_0 + t) - \theta(t_0)] \rangle \sim e^{-Dt}$ , as we have also done for the simulations of the theoretical model in the Main text. Examples of the decay of  $C(t)$  are shown in Figure 2. The obtained values of  $D$  lead to a precision of the order of  $p_{max} \sim 5 \times 10^2 s^{-1}$  and smaller by a factor  $\sim 10$  after 5 hours of oxygen deprivation, in full agreement with the results shown in the Main text.

- 
- [1] E. Lauga and T. R. Powers, Reports on Progress in Physics **72**, 096601 (2009).
  - [2] J. Elgeti, R. G. Winkler, and G. Gompper, Reports on

- Progress in Physics **78**, 056601 (2015).
- [3] L. J. Fauci and R. Dillon, Annual Review of Fluid Mechanics **38**, 371 (2006).

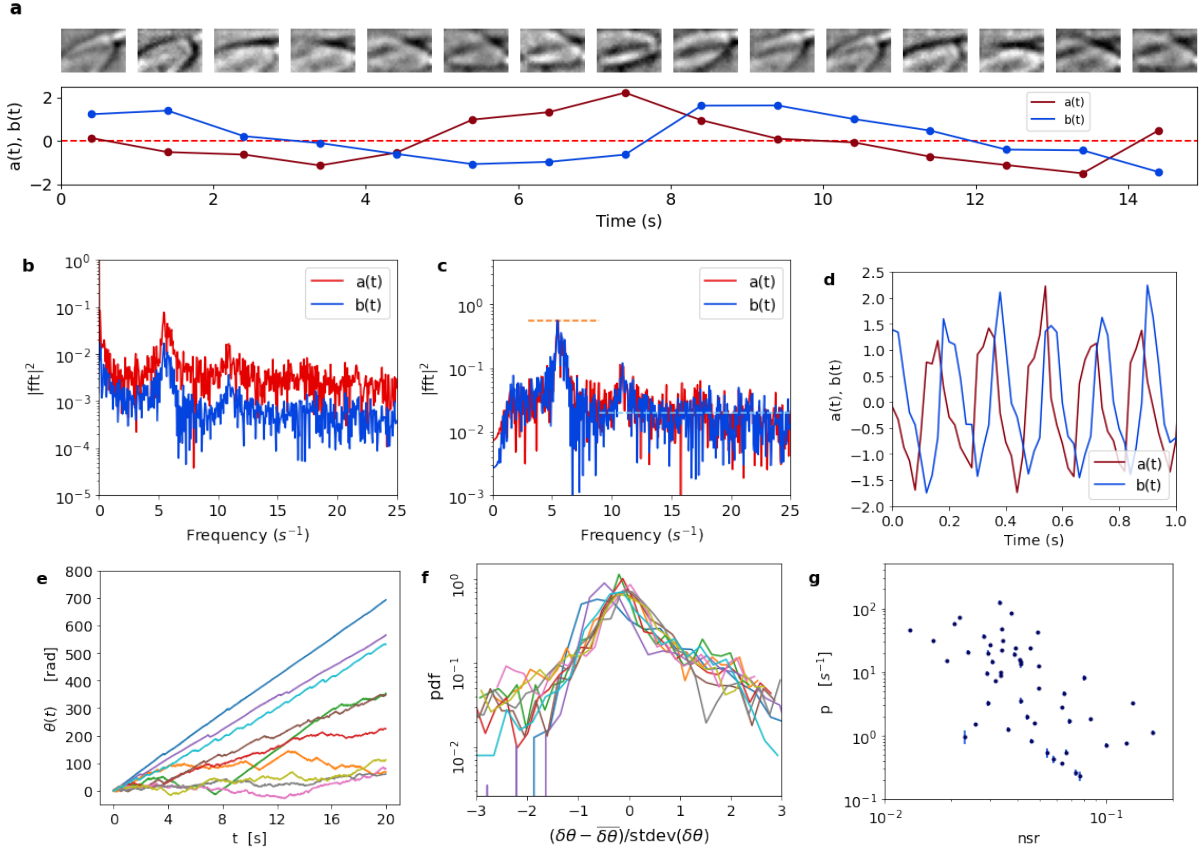


FIG. 8: Head tracking. **a**, Example of a head tracking where  $a(t)$  and  $b(t)$  (bottom plot) are obtained by computing the height ( $y$  position in the region of interest) of the center of mass of the pixel distribution and the slope of the direction associated with the maximum eigenvalue of the pixel covariance matrix. **b**, spectra of the signals  $a(t)$  and  $b(t)$ . **c**, spectra after signal filtering. The orange and light-blue dashed lines indicate the signal level and the noise level respectively. **d**, Examples of the signals  $a(t)$  and  $b(t)$  from head tracking: again  $a(t)$  anticipates  $b(t)$  of an angle between  $\sim \pi$  and  $\sim \pi/2$ . **e**, Integrated phase-space current  $\theta(t)$  for a few observed sperms. **f**, Pdf (over 20 seconds acquisition), for a few sperms, of  $\delta\theta = \theta(t + dt) - \theta(t)$  (shifted by the mean and scaled by the standard deviation), where  $dt = 0.02$  seconds. **g**, Precision  $p$  versus the noise-to-signal ratio (nsr) computed from the signals  $a(t)$  and  $b(t)$ . The sample size consists of 58 different observed sperm cells.

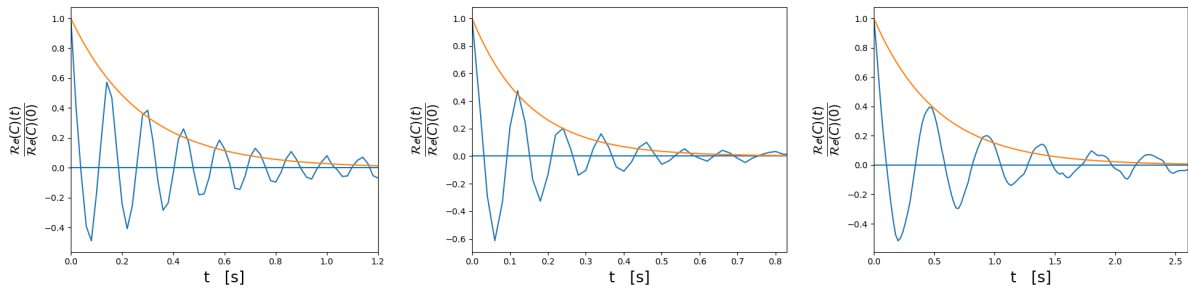


FIG. 9: Phase correlation decay for three different sperms in experiments. The first two are at the starting time of the experiment, while the third is after 150 minutes. The precisions measured are  $\sim 500s^{-1}$ ,  $\sim 400s^{-1}$  and  $\sim 80s^{-1}$ .

- [4] A. C. Tsang, E. Demir, Y. Ding, and O. S. Pak, Advanced Intelligent Systems **2**, 1900137 (2020).
- [5] C. B. Lindemann and K. A. Lesich, Cytoskeleton **73**, 652 (2016).
- [6] K. Machin, Journal of Experimental Biology **35**, 796 (1958).
- [7] J. Elgeti, U. B. Kaupp, and G. Gompper, Biophysical Journal **99**, 1018 (2010).
- [8] E. A. Gaffney, H. Gad  lha, D. J. Smith, J. R. Blake, and J. C. Kirkman-Brown, Annual Review of Fluid Mechanics **43**, 501 (2011).
- [9] H. C. Crenshaw, Biophysical journal **56**, 1029 (1989).

- [10] J. Gray and G. Hancock, *Journal of Experimental Biology* **32**, 802 (1955).
- [11] E. M. Purcell, *American Journal of Physics* **45**, 3 (1977).
- [12] F. Jülicher and J. Prost, *Physical review letters* **78**, 4510 (1997).
- [13] B. Friedrich and F. Jülicher, *New Journal of Physics* **10**, 123025 (2008).
- [14] B. M. Friedrich and F. Jülicher, *Physical Review Letters* **103**, 068102 (2009).
- [15] M. Polin, I. Tuval, K. Drescher, J. P. Gollub, and R. E. Goldstein, *Science* **325**, 487 (2009).
- [16] R. E. Goldstein, M. Polin, and I. Tuval, *Physical review letters* **103**, 168103 (2009).
- [17] R. E. Goldstein, M. Polin, and I. Tuval, *Physical Review Letters* **107**, 148103 (2011).
- [18] K. Y. Wan and R. E. Goldstein, *Physical review letters* **113**, 238103 (2014).
- [19] G. Quaranta, M.-E. Aubin-Tam, and D. Tam, *Physical review letters* **115**, 238101 (2015).
- [20] R. Ma, G. S. Klindt, I. H. Riedel-Kruse, F. Jülicher, and B. M. Friedrich, *Physical review letters* **113**, 048101 (2014).
- [21] G. S. Klindt and B. M. Friedrich, *Physical Review E* **92**, 063019 (2015).
- [22] A. Solovev and B. M. Friedrich, *Chaos: An Interdisciplinary Journal of Nonlinear Science* **32**, 013124 (2022).
- [23] A. C. Barato and U. Seifert, *Physical Review Letters* **114**, 158101 (2015).
- [24] T. R. Gingrich, J. M. Horowitz, N. Perunov, and J. L. England, *Physical Review Letters* **116**, 120601 (2016).
- [25] J. M. Horowitz and T. R. Gingrich, *Nature Physics* **16**, 15 (2020).
- [26] C. B. Lindemann, *Biophysical Journal* **84**, 4115 (2003).
- [27] D. T. Chen, M. Heymann, S. Fraden, D. Nicastro, and Z. Dogic, *Biophysical journal* **109**, 2562 (2015).
- [28] W. Gilpin, M. S. Bull, and M. Prakash, *Nature Reviews Physics* **2**, 74 (2020).
- [29] C. Bustamante, D. Keller, and G. Oster, *Accounts of Chemical Research* **34**, 412 (2001).
- [30] C. J. Brokaw, *Cell Motility and the Cytoskeleton* **66**, 425 (2009).
- [31] C. J. Brokaw, *Cell motility and the cytoskeleton* **53**, 103 (2002).
- [32] S. Burgess, *Journal of molecular biology* **250**, 52 (1995).
- [33] U. W. Goodenough and J. E. Heuser, *The Journal of cell biology* **95**, 798 (1982).
- [34] W. Hwang and C. Hyeon, *The Journal of Physical Chemistry Letters* **9**, 513 (2018).
- [35] G. Falasco and M. Esposito, *Physical Review Letters* **125**, 120604 (2020).
- [36] R. Rikmenspoel, G. Van Herpen, and P. Eijkhout, *Physics in Medicine & Biology* **5**, 167 (1960).
- [37] D. Woolley, *Reproduction* **126**, 259 (2003).
- [38] R. Nosrati, A. Driouchi, C. M. Yip, and D. Sinton, *Nature Communications* **6**, 1 (2015).
- [39] G. Saggiorato, L. Alvarez, J. F. Jikeli, U. B. Kaupp, G. Gompper, and J. Elgeti, *Nature Communications* **8**, 1 (2017).
- [40] C. Battle, C. P. Broedersz, N. Fakhri, V. F. Geyer, J. Howard, C. F. Schmidt, and F. C. MacKintosh, *Science* **352**, 604 (2016).
- [41] J. Gladrow, C. P. Broedersz, and C. F. Schmidt, *Physical Review E* **96**, 022408 (2017).
- [42] G. J. Stephens, B. Johnson-Kerner, W. Bialek, and W. S. Ryu, *PLoS Computational Biology* **4**, e1000028 (2008).
- [43] F. Gnesotto, F. Mura, J. Gladrow, and C. P. Broedersz, *Reports on Progress in Physics* **81**, 066601 (2018).
- [44] J. Li, J. M. Horowitz, T. R. Gingrich, and N. Fakhri, *Nature Communications* **10**, 1 (2019).
- [45] É. Roldán, J. Barral, P. Martin, J. M. Parrondo, and F. Jülicher, *New Journal of Physics* **23**, 083013 (2021).
- [46] C. Brokaw, *Science* **156**, 76 (1967).
- [47] R. Rikmenspoel, S. Sinton, and J. J. Janick, *The Journal of General Physiology* **54**, 782 (1969).
- [48] R. Rikmenspoel, *Journal of Experimental Biology* **108**, 205 (1984).
- [49] C. Brokaw, *Journal of Experimental Biology* **45**, 113 (1966).
- [50] C. Brokaw, *Journal of Experimental Biology* **62**, 701 (1975).
- [51] D. Nicastro, C. Schwartz, J. Pierson, R. Gaudette, M. E. Porter, and J. R. McIntosh, *Science* **313**, 944 (2006).
- [52] Z. Carvalho-Santos, J. Azimzadeh, J. B. Pereira-Leal, and M. Bettencourt-Dias, *The Journal of cell biology* **194**, 165 (2011).
- [53] G. S. Klindt, C. Ruloff, C. Wagner, and B. M. Friedrich, *Physical review letters* **117**, 258101 (2016).
- [54] N. Pellicciotta, E. Hamilton, J. Kotar, M. Faucourt, N. Delgehyr, N. Spassky, and P. Cicuta, *Proceedings of the National Academy of Sciences* **117**, 8315 (2020).
- [55] T. Guérin, J. Prost, and J.-F. Joanny, *The European Physical Journal E* **34**, 1 (2011).
- [56] T. Guérin, J. Prost, and J.-F. Joanny, *Physical Review E* **84**, 041901 (2011).
- [57] D. J. Skinner and J. Dunkel, *Proceedings of the National Academy of Sciences* **118** (2021).
- [58] X. Yang, M. Heinemann, J. Howard, G. Huber, S. Iyer-Biswas, G. Le Treut, M. Lynch, K. L. Montooth, D. J. Needleman, S. Pigolotti, et al., *Proceedings of the National Academy of Sciences* **118** (2021).
- [59] T. H. Tan, G. A. Watson, Y.-C. Chao, J. Li, T. R. Gingrich, J. M. Horowitz, and N. Fakhri, *arXiv preprint arXiv:2107.05701* (2021).
- [60] A. Samuël and H. C. Berg, *Proceedings of the National Academy of Sciences* **92**, 3502 (1995).
- [61] G. Vizsnyiczai, G. Frangipane, C. Maggi, F. Saglimbeni, S. Bianchi, and R. Di Leonardo, *Nature Communications* **8**, 15974 (2017).
- [62] J. Elgeti and G. Gompper, *EPL (Europhysics Letters)* **85**, 38002 (2009).
- [63] I. H. Riedel-Kruse, A. Hilfinger, J. Howard, and F. Jülicher, *HFSP journal* **1**, 192 (2007).
- [64] J. Howard, *Mechanics of Motor Proteins and the Cytoskeleton* (Sinauer Associates Inc, 2001).
- [65] L. Peliti and S. Pigolotti, *Stochastic Thermodynamics: An Introduction* (Princeton University Press, 2021).
- [66] Y. S. Kato, T. Yagi, S. A. Harris, S.-y. Ohki, K. Yura, Y. Shimizu, S. Honda, R. Kamiya, S. A. Burgess, and M. Tanokura, *Structure* **22**, 1628 (2014).
- [67] We remark that in this paper [34] cytoplasmic dynein is considered, which is known to be structurally similar to the axonemal one, with also a few distinct features [66].



# Thermodynamic limits of sperm swimming precision. SUPPLEMENTARY INFORMATION

## TRACKING THE HEAD OSCILLATIONS

In a series of experiments we have tracked the sperm's head instead of the tail, finding results in qualitative and quantitative agreement with those reported in the main article. The setup is identical, but different lighting and focus conditions with the microscope allowed us to have more image contrast in the interior of the cages. Images are collected with the same objective and ccd as in the main experiment. The region of interest is averagely the same area as in the main experiment. Background subtraction reduces the visibility of cage's boundaries. The covariance matrix of the pixel light distribution is computed: its eigenvector associated to the maximum eigenvalue determines the direction of orientation of the sperm's head, whose slope replaces coefficient  $-b(t)$  of our tail's analysis (the minus sign of course depends upon the reference frame we are using). The  $\hat{y}$  position of the center of mass of the head replaces coefficient  $a(t)$ . Once we get  $a(t), b(t)$  for the image at time  $t$  we can repeat exactly the same analysis as we did for the tail's tracking. In Figure 1 we summarise the results of this analysis.

## ALTERNATIVE ESTIMATES OF THE PRECISION

In a recent paper the fluctuations of the sperm beating cycle have been analysed [1]. The Authors suggest

two alternative ways to estimate the phase diffusivity  $D$  which is necessary to get values for  $p = J^2/D$  (being  $J = 2\pi f$  and  $f$  the average beating frequency). A first, perhaps more approximate, procedure is to retrieve the quality factor  $q = f_0/\Delta f_0$  where  $\Delta f_0$  is the width-at-half-maximum in the power spectrum, which reads  $\Delta f_0 \sim 3$  Hz giving  $q \approx 3$ . The quality factor is related to the phase diffusivity by  $q = J/(2D)$  which leads to  $p = J^2/D = 2Jq \approx 2 \times 10^2 s^{-1}$  which is compatible in order of magnitude with the maximum precision we report in the main text. The second recipe consists in measuring the decay in time of the phase correlation  $C(t) = \langle \exp i[\theta(t_0 + t) - \theta(t_0)] \rangle \sim e^{-Dt}$ , as we have also done for the simulations of the theoretical model in the Main text. Examples of the decay of  $C(t)$  are shown in Figure 2. The obtained values of  $D$  lead to a precision of the order of  $p_{max} \sim 5 \times 10^2 s^{-1}$  and smaller by a factor  $\sim 10$  after 5 hours of oxygen deprivation, in full agreement with the results shown in the Main text.

- 
- [1] R. Ma, G. S. Klindt, I. H. Riedel-Kruse, F. Jülicher, and B. M. Friedrich, Physical review letters **113**, 048101 (2014).

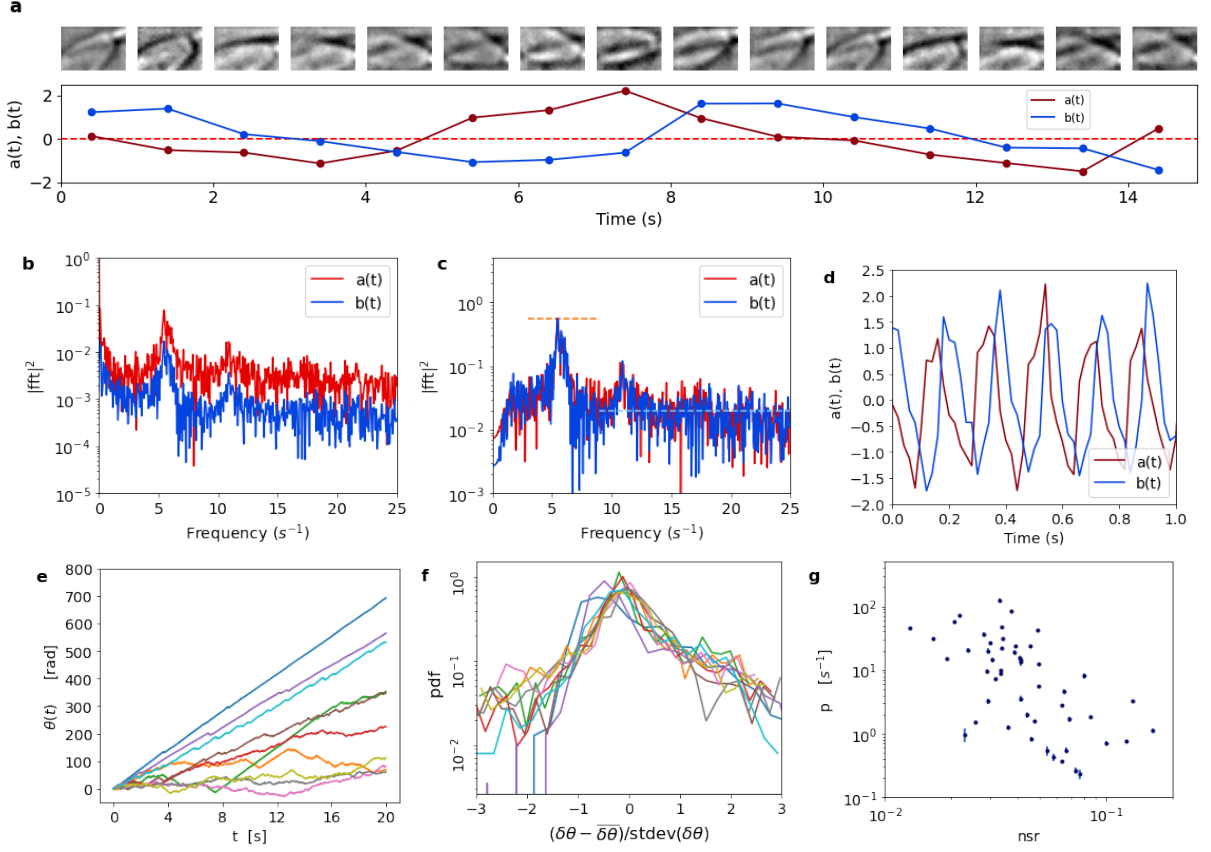


FIG. 1: Head tracking. **a**, Example of a head tracking where  $a(t)$  and  $b(t)$  (bottom plot) are obtained by computing the height ( $y$  position in the region of interest) of the center of mass of the pixel distribution and the slope of the direction associated with the maximum eigenvalue of the pixel covariance matrix. **b**, spectra of the signals  $a(t)$  and  $b(t)$ . **c**, spectra after signal filtering. The orange and light-blue dashed lines indicate the signal level and the noise level respectively. **d**, Examples of the signals  $a(t)$  and  $b(t)$  from head tracking: again  $a(t)$  anticipates  $b(t)$  of an angle between  $\sim \pi$  and  $\sim \pi/2$ . **e**, Integrated phase-space current  $\theta(t)$  for a few observed sperms. **f**, Pdf (over 20 seconds acquisition), for a few sperms, of  $\delta\theta = \theta(t + dt) - \theta(t)$  (shifted by the mean and scaled by the standard deviation), where  $dt = 0.02$  seconds. **g**, Precision  $p$  versus the noise-to-signal ratio (nsr) computed from the signals  $a(t)$  and  $b(t)$ . The sample size consists of 58 different observed sperm cells.

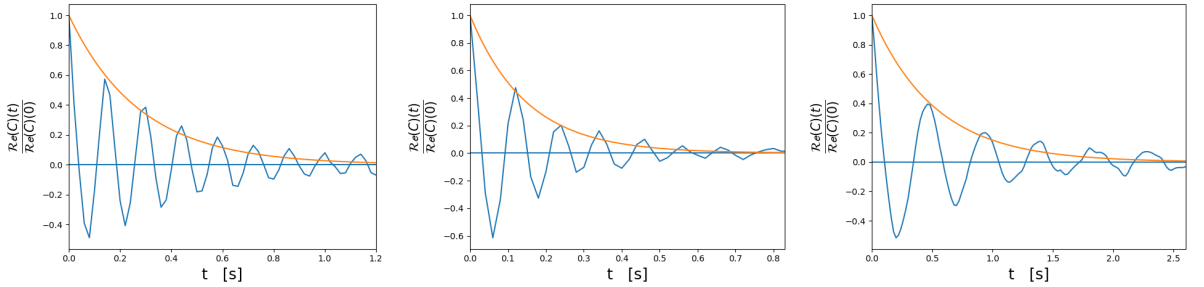


FIG. 2: Phase correlation decay for three different sperms in experiments. The first two are at the starting time of the experiment, while the third is after 150 minutes. The precisions measured are  $\sim 500s^{-1}$ ,  $\sim 400s^{-1}$  and  $\sim 80s^{-1}$ .